Research and Improvement of Oscillation Problems Caused by Active Rectifier Circuits in EV-WPT Systems

Haoze Li, *Student Member, IEEE*, Linlin Tan, *Member, IEEE*, Ruoyin Wang, *Student Member, IEEE*, and Xueliang Huang, *Member, IEEE*

***Abstract*—In the secondary side of the wireless power transfer system, the active rectifier helps increase efficiency and adjust output characteristics. However, there is a certain probability that oscillation problems will occur, especially in an *LCC-LCC* system. A closed loop that causes oscillations in the circuit is figured out. And with the established discrete system mode, the dynamic oscillation conditions are presented in a wide operating range. The theory and simulation show that the proposed improved control method based on the resonant filter breaks the original oscillation closed loop and effectively suppresses oscillations. Finally, the proposed method is applied in an experimental prototype, and the stable operating range of the improved prototype is significantly expanded.**

***Index Terms*—Active rectifier, current oscillation, reflected current, synchronous modulation, wireless power transfer (WPT).**

I. Introduction

WIRELESS power transfer (WPT) technology has received a lot of attention as a noncontact charging method. The great advantages in terms of safety, convenience, and flexibility have led to the rapid development of research and applications of WPT technology in recent years in smartphones [1], mobile cloud computing [2], implantable medical devices [3], autonomous guided vehicles [4], [5], and electric vehicles [6], [7]. In magnetically coupled WPT systems, energy is transferred from the primary side to the secondary side through the high-frequency magnetic field between the coupling coils. The resonant compensation network in this kind of system greatly improves the efficiency of the WPT system by providing reactive power to the coupling coils [8], [9]. Among several types of compensation topologies (e.g., S-S, *LCC*-S, *LCC-LCC*), the *LCC-LCC* resonant network is widely used because the characteristics of constant primary-side coil current and constant secondary-side output current make it safe and easy to control [10], [11].

In addition, active rectifiers are receiving more and more attention in the secondary side circuit to achieve higher efficiency and good dynamic performance in WPT systems. Compared to diode rectifier bridges, active rectifiers not only reduce losses [12], but also enable output characteristic control (constant voltage, constant current, or power control) and impedance matching by operating the conduction angle, thus saving additional dc–dc converters [13]. Literature [14], [15], [16], [17], [18] give research works on controlled rectification in terms of circuit topology, control logic of switching tubes, and closed-loop control strategies, which have achieved good experimental results. Accurate control of the conduction angle is a prerequisite for the stable and efficient operation of the active rectifier, for which an accurate synchronization signal of the output current of the resonant network on the secondary side is required as a reference. The conventional method is to use a current sensor and a comparator to generate the synchronization signal, and the literature [17], [19], [20] have made some explorations for the synchronization signal acquisition and phase locking methods.

It was found that in a WPT system using an *LCC-LCC* network, the input current of the active rectifier system oscillates when the active rectifier operates within a specific conduction angle and load range if a conventional synchronous control strategy is used [21]. Oscillations limit the effective operating range, make the switching timing of power devices invalid, cause peak misalignment of the current, and drastically reduce the lifetime of the device [22]. Severe oscillations can lead to a complete loss of circuit control.

At present, there are few studies in the field of WPT for the oscillation problem, mostly focusing on synchronization techniques. For example, Thrimawithana et al. [23], Liu et al. [24], and Tang et al. [25] proposed novel accurate synchronization methods to avoid the appearance of oscillations. In [26], the current distortion caused by harmonics in the *LCC-LCC* system is analyzed and an improved method is proposed. However, the relationship between distortion and oscillation is not mentioned. Only in [21], the oscillation problem is mentioned and the law of circuit conductance and harmonics of the oscillation current is analyzed, but the mechanism of oscillation occurrence is not given. Currently, the cause of oscillation generation has not been clarified and this is the problem that this article is dedicated to.

Manuscript received 7 March 2023; revised 13 May 2023 and 26 June 2023; accepted 10 July 2023. Date of publication 17 July 2023; date of current version 1 September 2023. This work was supported in part by the Qing Lan Project of Jiangsu, in part by the National Key Research and Development Project under Grant 2021YFB2501604, and in part by the Project of Jiangsu Provincial Key Laboratory of Smart Grid Technology and Equipment, Southeast University. Recommended for publication by Associate Editor M. Vitelli. *(Corresponding author: Linlin Tan.)*

The authors are with the School of Electrical Engineering, Southeast University, Nanjing 210096, China (e-mail: 230218321@seu.edu.cn; tanlinlin@seu.edu.cn; ruoy_wang@yahoo.com; xlhuang@seu.edu.cn).

Color versions of one or more figures in this article are available at https://doi.org/10.1109/TPEL.2023.3295841.

Digital Object Identifier 10.1109/TPEL.2023.3295841

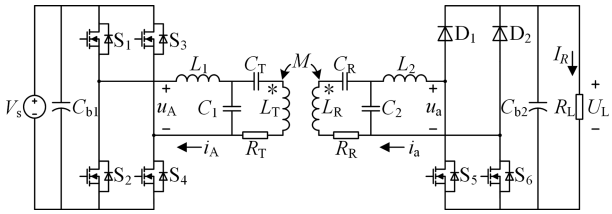

Fig. 1. Schematic of the *LCC-LCC* wireless charging system.

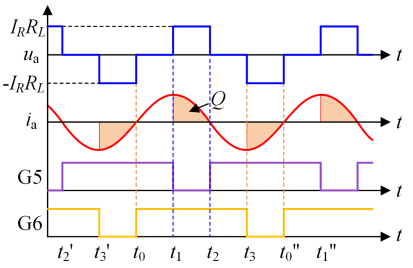

Fig. 2. Switch timings of S5 and S6.

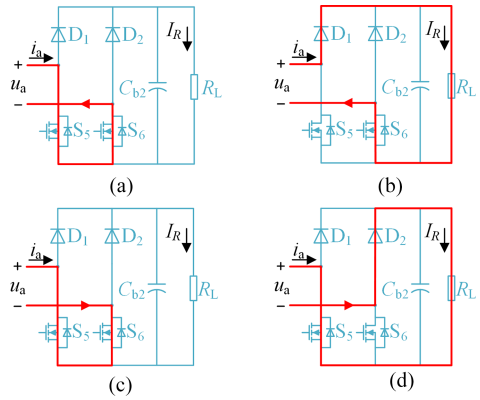

Fig. 3. Four working states of the active rectifier.

To fill this research gap, in this article, the generation of oscillations in the *LCC-LCC* system is reasoned in terms of the reflected current on the secondary side. A closed-loop model for the formation of oscillations is established. The mechanism of the continuous interaction of current and voltage within the closed loop is specifically elucidated, and the factors affecting the intensity of oscillations are analyzed. On this basis, an improved method of adding a resonant filter after the current sensor is proposed, which can change the original closed loop and, thus, suppress oscillations, effectively avoiding additional losses and heat generation caused by adding filter components in the power loop. Thanks to the improved method, the operating range of the active rectifier is greatly extended. This innovative measure helps to realize a wider application of active rectifiers in WPT systems. Finally, a prototype was built to verify the practical effect of the added resonant filter. With the improved method, the oscillation phenomenon was extensively eliminated and the operation in CV mode with higher voltage was possible.

The rest of this article is organized as follows. Section II describes the operation mode of the active rectifier in the WPT system and the conventional synchronous control method. Section III exposes the effect of reflected current and the formation of oscillation loops, and further gives the oscillations over a wide operating range using a discrete model established. In Section IV, an improved control method based on an additional resonant filter is proposed and its feasibility is confirmed by control group simulations. In Section V, experimental results from a prototype verify the improved effectiveness of the proposed method. Finally, Section VI concludes this article.

II. Active Rectifier in a WPT System

To explain the oscillation problem in the WPT system, the application of an active rectifier in the WPT system is explained first. In this section, the schematic and parameters of the circuit are shown in Fig. 1, and the working principle of the conventional synchronous control method of the active rectifier circuit is explained in detail.

A. Schematic and Parameters

Fig. 1 shows the schematic diagram of the wireless charging system with the *LCC-LCC* compensation network. On the primary side of the system, a full-bridge inverter consisting of four MOSFETS (S_1 –S_4) converts the supply voltage *Vs* to an ac square wave voltage u_A with frequency f_0. The active rectifier consisting of two diodes (D_1, D_2) and two MOSFETS (S_5, S_6) is used on the secondary side of the system. i_a and u_a are the input current and voltage of the active rectifier, respectively.

B. Conventional Synchronous Control Method

The timing of the drive signals (G5, G6) of S_5 and S_6 under the conventional synchronous control method is shown in Fig. 2. And their operating states can be divided into four time periods within one cycle, as shown in Fig. 3.

t_0-t_1: i_a is positive, S_5 turns ON, and the current flows from the drain to the source, while S_6 makes synchronous rectification, as shown in Fig. 3(a).

t_1-t_2: i_a is positive, S_5 is turned OFF, S_6 makes synchronous rectification, and the current flows through R_L, as shown in Fig. 3(b).

t_2-t_3: i_a is negative, S_5 makes synchronous rectification, while S6 turns ON, and the current flows from the drain to the source, as shown in Fig. 3(c).

t_3-t_0": i_a is negative, S_5 makes synchronous rectification, S_6 turns OFF, and the current flows through R_L, as shown in Fig. 3(d).

The active rectifier circuit transfers the secondary-side input power to the load only during the periods t_1-t_2 and t_3-t_0". In Fig. 2, the shaded area represents the amount of charge Q transferred during this period, and it is easy to conclude that the filtered output current I_R is

$$I_R = 2f_0 \int_{t_1}^{t_2} i_a dt. \tag{1}$$

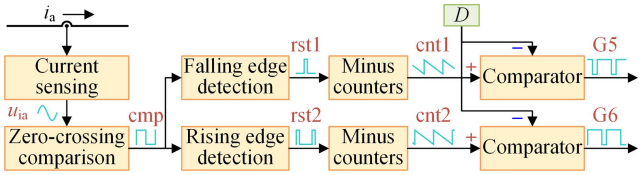

Fig. 4. Method of synchronous PWM modulation.

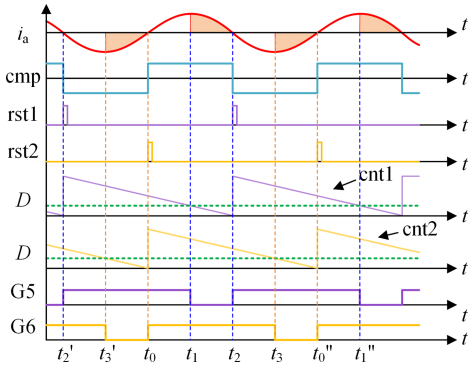

Fig. 5. Waveforms of synchronous PWM modulation.

Equation (1) illustrates that the value of I_R can be adjusted by changing the moment of t_1. To achieve this, a synchronous PWM modulation method is commonly used in active rectifiers to generate G5 and G6, as shown in Fig. 4. The process of this method is as follows.

1) Use a current sensing chip to detect i_a in real-time and convert it to the corresponding voltage signal u_{ia}.
2) Perform a zero-crossing comparison of u_{ia} to obtain the square wave signal cmp.
3) Use edge detection to obtain the signal rst1 that triggers the pulse on the falling edge of cmp and the signal rst2 that triggers the pulse on the rising edge of cmp.
4) Two counters with initial value N, step size -1 and counting frequency f_s with high reset are reset by rst1 and rst2, respectively, and the corresponding output signals are cnt1 and cnt2.
5) Cnt1 and cnt2 are modulated by two comparators with a given value D to obtain G5 and G6, where $0 \le D \le N/2$.

The waveforms and timings of each signal in the abovementioned process are shown in Fig. 5 where the counter should satisfy

$$N = f_s/f_0. \tag{2}$$

Under the constraint of (2), both cnt1 and cnt2 are sawtooth waves, and it can be derived that

$$t_1 = t'_2 + (N - D)/Nf_0. \tag{3}$$

Set the current i_a as a sine wave, and the instantaneous expression is

$$i_a(t) = I_a \sin(\omega_0 t + \varphi_0) \tag{4}$$

where I_a is the amplitude, $\omega_0 = 2\pi f_0$, and φ_0 is the initial phase.

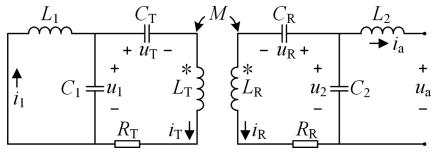

Fig. 6. Equivalent circuit when only u_a is applied.

Then, the relationship between I_R and D is obtained by combining (1), (3), and (4) as follows:

$$I_R = \frac{I_a}{\pi}\left(1 - \cos\frac{2\pi D}{N}\right). \tag{5}$$

At this point, the principle of synchronous PWM modulation of active rectifiers has been completely introduced and it is clearly illustrated how the I_R can be regulated by controlling D.

III. Analysis of Oscillation Problems

A. Effect of Reflected Current

In a WPT system with a rectifier circuit on the secondary side, i_a is not an ideal sine wave. The reflected current generated by the rectifier distorts i_a, which is a key prerequisite for the formation of oscillations. In this part, the steady-state waveform of i_a will be analyzed with the help of the Fourier series.

According to the superposition theorem, i_a is excited by u_A and u_a together. The contribution of which u_A is denoted as i_{a1} and the reflected current of the rectifier contributed by u_a is denoted as i_{a2}. And so there is

$$i_a = i_{a1} + i_{a2}. \tag{6}$$

First, the contribution of u_A is analyzed. As a square wave voltage, u_A contains harmonic components. However, since the *LCC-LCC* network exhibits the characteristics of a high-order filter from the primary to the secondary side, the effect of harmonic components can be neglected, making i_{a1} contain only fundamental components [10]. Thus, the phasor expression of i_{a1} is

$$\dot{I}_{a1} = -j\frac{M\dot{U}_A^{(1)}}{\omega_0 L_1 L_2}. \tag{7}$$

Second, the contribution of u_a is analyzed. The prestage circuit of the active rectifier is equated to a single-port network, as shown in Fig. 6, and the conduction Y_a of this network is deduced as

$$\begin{cases} Z_1 = R_T + j\omega L_T + \frac{1}{j\omega C_T} + \frac{1}{j\omega C_1 + 1/j\omega L_1} \\ Z_{12} = \omega^2 M^2 / Z_1 \\ Z_a = j\omega L_2 + \frac{1}{j\omega C_2 + \frac{1}{R_R + j\omega L_R + 1/j\omega C_R + Z_{12}}} \\ Y_a = 1/Z_a. \end{cases} \tag{8}$$

Then, because of the large capacitance of C_{b2} on the output side of the active rectifier, and the clamping effect of the diode and MOSFET during conduction, u_a is presented as a step wave with amplitude approximating $I_R R_L$, as shown in Fig. 2. Thus, u_a can be expanded in the interval [−T/2, T/2] with t_0 as the

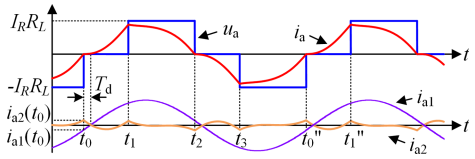

Fig. 7. Waveforms when the active rectifier is applied in the *LCC-LCC* system.

coordinate origin by the Fourier series as

$$u_{\mathrm{a}}(t) \sim -\frac{4I_R R_L}{\pi}\sum_{n=1}^{\infty}\frac{1}{n}\sin\frac{nD\pi}{N}\cos\left(n\omega_0 t+\frac{nD\pi}{N}\right) \quad (9)$$

where $n = 1, 3, 5\ldots$.

Further derivation of $i_{\mathrm{a2}}(t)$ with t_0 as the origin is

$$i_{\mathrm{a2}}(t) \sim \frac{4I_R R_L}{\pi}\sum_{n=1}^{\infty}\frac{Y_{\mathrm{a}}^{(n)}}{n}\sin\frac{nD\pi}{N}\cos\left(n\omega_0 t+\frac{nD\pi}{N}\right) \quad (10)$$

where $Y_a^{(n)}$ is Y_{a} when the frequency is nf_0, and $n = 1, 3, 5\ldots$.

And according to (7), $i_{\mathrm{a1}}(t)$ with t_0 as the origin is derived

$$i_{\mathrm{a1}}(t) = \frac{\sqrt{2}MU_{\mathrm{A}}^{(1)}}{\omega_0 L_1 L_2}\sin\omega_0(t-T_{\mathrm{d}}) \quad (11)$$

where T_{d} is the time at which the zero-crossing moment (t_{c}) of i_{a1} lags behind t_0.

Since t_0 is a zero-crossing moment of i_{a}, the sum of $i_{\mathrm{a1}}(t_0)$ and $i_{\mathrm{a2}}(t_0)$ is 0. And the expression about T_{d} can be derived according to (10), (11)

$$\sin(\omega_0 T_{\mathrm{d}}) = \frac{\sqrt{2}\omega_0 I_{\mathrm{R}} R_{\mathrm{L}} L_1 L_2}{\pi M U_{\mathrm{A}}^{(1)}}\sum_{n=1}^{\infty}\frac{Y_{\mathrm{a}}^{(n)}}{n}\sin\frac{2nD\pi}{N}. \quad (12)$$

It can be seen by (12) that t_0 coincides with t_{c} when $D = 0$; t_0 overruns t_{c} when $D > 0$. This indicates that when the active rectifier outputs current, the zero-crossing point of i_{a} must be offset from the zero-crossing point of i_{a1} due to the presence of i_{a2}, as shown in Fig. 7. And the offset T_{d} is determined by several variables together, including u_{A}, u_{a}, and the parameters of the resonant network.

B. Oscillation Loop

The phenomenon of zero-crossing shift makes the conventional synchronous control method lack a stable reference phase, which in turn makes it impossible to output accurate PWM signals. This makes a closed loop in the circuit that makes u_{a} and i_{a} interact with each other. According to the analysis abovementioned, i_{a2} is the sum of the higher harmonics in the frequency domain. However, the waveform during oscillations is difficult to analyze in the frequency domain. Therefore, this section will explain it specifically in conjunction with the transient response of the system.

Consider the circuit shown in Fig. 6 as a linear system with u_{a} as input and i_{a2} as output. In the time domain, i_{a2} should be considered as an alternation of step response and free response, since u_{a} is an intermittent step input. Specifically, in Fig. 5, the periods of free response are t_0-t_1 and t_2-t_3, and the periods of step response are t_1-t_2 and t_3-t_0".

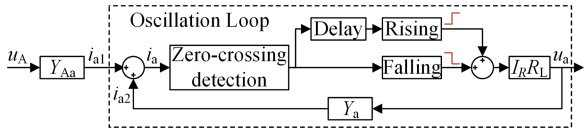

Fig. 8. Closed loop between u_{a} and i_{a}.

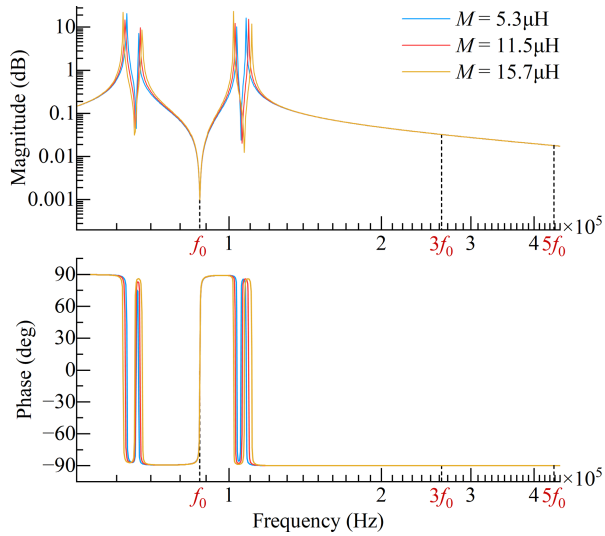

Fig. 9. Frequency characteristics of Y_{a} with different M.

On the other hand, the conventional modulation makes all rising and falling edges of u_{a} depend directly on the zero-crossing phase of i_{a}. Taking the moments t_1 and t_2 as examples. First, t_2 is the moment when i_{a2} drops under the step input from the moment t_1 to the moment when i_{a} drops to zero, as shown in Fig. 7. The zero-crossing of i_{a} makes u_{a} fall back naturally with the cutoff of D1. Second, according to (3), it is clear that the moment of t_1 is determined by the moment of t_2', and similarly, the moment of t_1" is determined by the moment of t_2. Therefore, i_{a2} determines both the moment of fallback of u_{a} in the current cycle (t_2) and the moment of u_{a} stepping toward positive voltage in the next cycle (t_1"). It is similar for the negative half-cycle of i_{a}.

Fig. 8 visualizes the mathematical model of the secondary side circuit, and it is clear that a closed loop is formed in the system where u_{a} and i_{a} interact periodically. This closed loop allows the fluctuations of the system to be continuously conducted with the cycle, resulting in a weaker convergence to the steady state. Moreover, with a constant primary-side voltage u_{A}, the larger the value of the load RL, the larger the u_{a}, and the larger the percentage of the reflected current in i_{a}. And, then, the more significant the effect of the closed loop. Therefore, in practice, as the load increases, the more difficult it is for the system to maintain a steady state, and distinct periodic oscillations occur when the load is greater than a specific threshold.

In addition, the magnetic coupling condition is variable when the coil position is shifted or it is in dynamic WPT systems. This brings about a change in the mutual inductance between the primary and secondary side coils and Y_{a} also changes according to (8). Since Y_{a} affects i_{a2} in the oscillation loop, it is

TABLE I
PARAMETERS OF THE RESONANT NETWORK

Symbol	Parameter	Value
L_T	Primary side coil inductance	104.5 μH
L_R	Secondary side coil inductance	92.9 μH
R_T	Internal resistance of the primary side coil	0.12 1Ω
R_R	Internal resistance of the Secondary side coil	0.13 1Ω
L_1	Primary side compensated inductance	20 μH
L_2	Secondary side compensated inductance	21 μH
C_1	Primary side compensation capacitor	165.4 2nF
C_2	Secondary side compensation capacitor	157.55 nF
C_T	Primary side resonant capacitor	39.15 nF
C_R	Secondary side resonant capacitor	46.01 nF
f_0	Resonant frequency	87.5 kHz
M	Mutual inductance	11 μH

possible that the oscillation situation also changes accordingly. Fig. 9 shows the frequency response of Y_a under three mutual inductances based on the actual relative positions of the coils. As can be seen from Fig. 9, the frequency response curves under different mutual inductances coincide exactly at the fundamental frequency and frequencies above the third harmonic. And according to (10), i_{a2} consists of the fundamental wave and odd harmonics. Therefore, the variation of mutual inductance does not affect the oscillation loop. So that there is no correlation between the magnetic coupling condition and the oscillation.

C. Modeling and Simulation

In order to clarify the variation law of the oscillation phenomenon with the influencing factors, the discrete model of the active rectifier in the system with *LCC-LCC* compensation is established and simulated in this section. The parameters of the resonant network are shown in Table I. The state space expression of the bilateral *LCC* network is used to calculate the transient response of i_{a2} to u_a. A system of differential equations is written according to Kirchhoff's voltage law and Kirchhoff's current law as follows:

$$\begin{cases} u_1 = -L_1\dot{i}_1 \\ u_1 = u_T + L_T\dot{i}_T + R_T i_T + M\dot{i}_R \\ i_T = C_T\dot{u}_T \\ i_1 = i_T + C_1\dot{u}_1 \\ u_a = -L_2\dot{i}_2 + u_2 \\ i_a = -i_R - C_2\dot{u}_2 \\ i_R = C_R\dot{u}_R \\ u_2 = u_R + L_R\dot{i}_R + R_R i_R + M\dot{i}_T \end{cases} \tag{13}$$

where the meanings and reference directions of the variables are shown in Fig. 6.

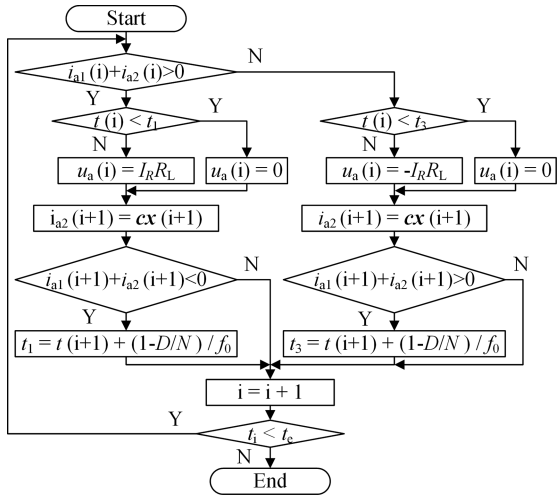

Fig. 10. Flowchart of the discrete model.

With u_a as input and i_{a2} as output, the state space expression is organized according to (13)

$$\begin{aligned} \dot{\boldsymbol{x}}_1 &= \boldsymbol{A}_1\boldsymbol{x}_1 + \boldsymbol{b}u_a \\ y &= \boldsymbol{c}\boldsymbol{x}_1 \end{aligned} \tag{14}$$

where (15) shown at the bottom of this page

$$\boldsymbol{b} = \begin{bmatrix} 0 & 0 & 0 & 0 & -1/L_2 & 0 & 0 & 0 \end{bmatrix} \tag{16}$$

$$\boldsymbol{c} = \begin{bmatrix} 0 & 0 & 0 & 0 & 1 & 0 & 0 & 0 \end{bmatrix} \tag{17}$$

$$\boldsymbol{x}_1 = \begin{bmatrix} i_1 & u_1 & i_T & u_T & i_{a2} & u_2 & i_R & u_R \end{bmatrix} \tag{18}$$

$$K = L_T L_R - M^2. \tag{19}$$

Then, the discrete i_{a2} is derived from the state space

$$\begin{aligned} i_{a2}(\mathrm{i}+1) &= \boldsymbol{c}\boldsymbol{x}_1(\mathrm{i}+1) \\ &= \boldsymbol{c}\left[e^{\boldsymbol{A}t_s}\boldsymbol{x}_1(\mathrm{i}) + \boldsymbol{A}_1^{-1}\left(e^{\boldsymbol{A}t_s} - \boldsymbol{I}\right)\boldsymbol{b}u_a(\mathrm{i})\right] \end{aligned} \tag{20}$$

where t_s is the sampling time of the discrete model.

A discrete secondary-side circuit operation model is designed according to the system block diagram shown in Fig. 8, and the waveform of i_a can be simulated for a given initial state $x(0)$ and time t_e. The flowchart of the model is shown in Fig. 10, and the procedure of the calculation is as follows. Within each loop, the current u_a(i) is determined by first judging the direction of the current i_a(i) and further judging whether the current time

$$\boldsymbol{A}_1 = \begin{bmatrix} 0 & -1/L_1 & 0 & 0 & 0 & 0 & 0 & 0 \\ 1/C_1 & 0 & -1/C_1 & 0 & 0 & 0 & 0 & 0 \\ 0 & \frac{L_R}{K} & -\frac{L_R R_T}{K} & -\frac{L_R}{K} & 0 & -\frac{M}{K} & \frac{MR_R}{K} & \frac{M}{K} \\ 0 & 0 & 1/C_T & 0 & 0 & 0 & 0 & 0 \\ 0 & 0 & 0 & 0 & 0 & 1/L_2 & 0 & 0 \\ 0 & 0 & 0 & 0 & -1/C_2 & 0 & -1/C_2 & 0 \\ 0 & -\frac{M}{K} & \frac{MR_T}{K} & \frac{M}{K} & 0 & \frac{L_T}{K} & -\frac{L_T R_R}{K} & -\frac{L_T}{K} \\ 0 & 0 & 0 & 0 & 0 & 0 & 1/C_R & 0 \end{bmatrix} \tag{15}$$

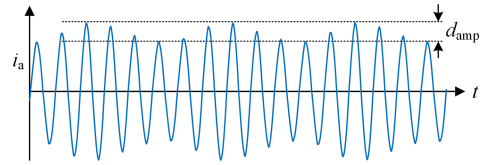

Fig. 11. Example of the waveform of i_a when oscillation occurs and the illustration of d_{amp}.

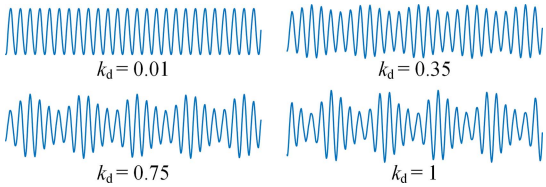

Fig. 12. Waveforms of i_a with four different degrees of oscillation.

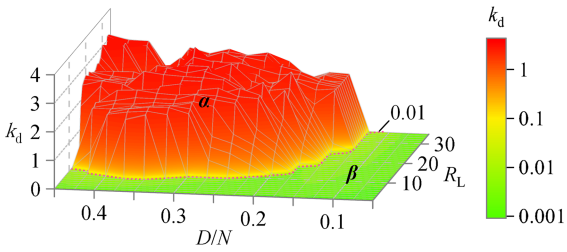

Fig. 13. Values of the simulated k_d for the original system.

t(i) reaches t_1 or t_3. Subsequently, i_{a2}(i + 1) is calculated for the next cycle according to (20). And if i_a(i + 1) is reversed from i_a(i), then t_1 or t_3 of the next cycle is updated according to (3) before executing the next cycle, otherwise, the next cycle starts directly.

A typical oscillation waveform of i_a is shown in Fig. 11, and the difference in amplitude fluctuations is denoted as d_{amp}. In applications, *D*/*N* and R_L are two key parameters that affect the oscillation of the circuit. Therefore, the circuits corresponding to all *D*/*N* and R_L combinations within a specified range are simulated. Specifically, for the current system parameters, *D*/*N* is taken from 0.05 to 0.45 with an interval of 0.025, and R_L is taken from 1 Ω to 35 Ω with an interval of 1 Ω. k_d is introduced to characterize the degree of oscillation of the simulated i_a and is denoted as

$$k_d = d_{amp}/I_{a1}. \tag{21}$$

Fig. 12 shows the waveforms of i_a with four different oscillation degrees in the simulation results. It is easy to see that k_d is positively related to the degree of oscillation, and there is no significant oscillation for i_a with k_d of 0.01.

The values of k_d corresponding to all combinations are plotted as surface plots in Fig. 13, which are sharply divided into two regions according to the degree of oscillation. These are the region α where the oscillations are severe and the region β where the operation is stable (in this article, $k_d \leq 0.01$ is used as the stability criterion). Moreover, it can be seen that for a fixed *D*/*N*, the oscillations appear and intensify gradually with the increase of the load. And each value of *D*/*N* has a corresponding critical load for the emergence of oscillations. Obviously, the oscillation problem in the α region greatly limits the available operating range.

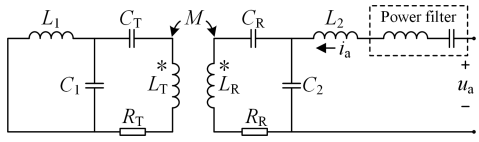

Fig. 14. Power filter in the resonant network.

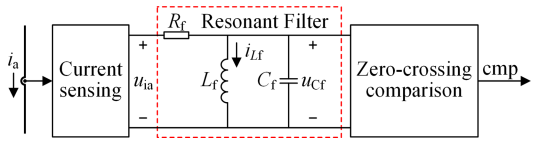

Fig. 15. Additional resonant filter after the current sensor.

IV. Improved Control Method

To improve the oscillation problem in *LCC-LCC* systems, a control method for active rectifiers based on additional resonant filters is proposed. The method aims to break the closed loop of oscillations in the circuit and avoid oscillations from the principle.

A. Additional Resonant Filter

According to the previous analysis, the reflected current i_{a2} is the key factor in the formation of oscillation, so reducing i_{a2} is a reasonable improvement. And this requires a filter to be connected in series with the power circuit to reduce $Y_a(\omega)$ at the harmonic frequency, as shown in Fig. 14. However, there is the disadvantage of generating additional losses resulting in lower efficiency. To avoid adverse effects on power transfer, a method is proposed to modify only the synchronous PWM modulation. A resonant filter is introduced behind the current sensing circuit, as shown in Fig. 15. The filter consists of a series-connected resistor R_f, a parallel-connected inductor L_f, and a capacitor C_f. u_{ia} is the current sensing signal of i_a as the input of the filter and the voltage u_{Cf} of C_f as the output of the filter. The relationship between L_f and C_f is

$$L_f C_f = 1/\omega_0^2. \tag{22}$$

And the gain of the filter concerning frequency is

$$G_{pf}(\omega) = 1 - \frac{(\omega_0^2 - \omega^2)}{(\omega_0^2 - \omega^2) + j\omega_0^2 \omega p} \tag{23}$$

where $p = L_f/R_f$.

According to (23), it can be known that the gain at ω_0 is 1 and the attenuation on both sides is determined by p. From (11), it can be seen that i_{a1} is the component of ω_0 frequency. Fig. 9 shows that the fundamental frequency component of Y_a is particularly small. Thus, i_{a2} is mainly the harmonic component. Thus, the introduced filter can retain the part of i_{a1} in u_{ia} and attenuate the part of i_{a2}. When the attenuation is large enough, almost only the

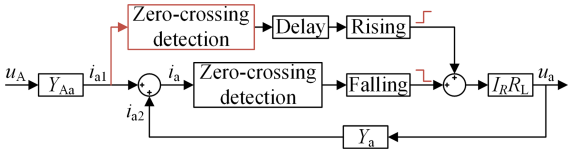

Fig. 16. Improved ideal equivalent system block diagram.

i_{a1} component remains in the output of the filter, and the system block diagram is equivalent to that shown in Fig. 16. Compared to the original block diagram in Fig. 8, the rising edge signal of u_a becomes directly based on the zero-crossing signal of i_{a1} and is no longer affected by the closed loop between i_a and u_a after the filter is added. This improvement can effectively suppress oscillations.

B. Effect of the Additional Resonant Filter

To verify the feasibility of the improved method in principle, a discrete model of the system with resonant filters is developed. The state space is expanded based on (14) for the changes in the system

$$\begin{bmatrix}\dot{\boldsymbol{x}}_1\\ \dot{\boldsymbol{x}}_2\end{bmatrix} = \begin{bmatrix}\boldsymbol{A}_1 & \boldsymbol{0}\\ \boldsymbol{A}_{21} & \boldsymbol{A}_{22}\end{bmatrix}\begin{bmatrix}\boldsymbol{x}_1\\ \boldsymbol{x}_2\end{bmatrix} + \boldsymbol{b}u_a$$
$$\boldsymbol{y} = \begin{bmatrix}\boldsymbol{c}_1\\ \boldsymbol{c}_2\end{bmatrix}\begin{bmatrix}\boldsymbol{x}_1\\ \boldsymbol{x}_2\end{bmatrix} \tag{24}$$

where

$$\boldsymbol{A}_{21} = \begin{bmatrix}0 & 0 & 0 & 0 & 0 & 0 & 0 & 0\\ 0 & 0 & 0 & 0 & 1/(C_f R_f) & 0 & 0 & 0\end{bmatrix} \tag{25}$$

$$\boldsymbol{A}_{22} = \begin{bmatrix}0 & 1/L_f\\ -1/C_f & -1/(C_f R_f)\end{bmatrix} \tag{26}$$

$$\boldsymbol{c}_1 = \begin{bmatrix}0 & 0 & 0 & 0 & 1 & 0 & 0 & 0 & 0 & 0\end{bmatrix} \tag{27}$$

$$\boldsymbol{c}_2 = \begin{bmatrix}0 & 0 & 0 & 0 & 0 & 0 & 0 & 0 & 0 & 1\end{bmatrix} \tag{28}$$

$$\boldsymbol{x}_2 = \begin{bmatrix}i_{L_f} & u_{C_f}\end{bmatrix}^T. \tag{29}$$

As the signal of i_{a2} after passing through a current sensor and filter, the $u_{Cf\,ia2}$ can be calculated by

$$u_{Cf\_ia2} = \boldsymbol{c}_2\begin{bmatrix}\boldsymbol{x}_1 & \boldsymbol{x}_2\end{bmatrix}^T. \tag{30}$$

Accordingly, the flow chart of the discrete model is changed to, as shown in Fig. 17. The calculation of $u_{Cf\,ia2\ (i\,+\,1)}$ is added in each loop, and t_1 or t_3 is updated when u_{Cf} crosses zero. The p-parameter of the additional filter determines the suppression of oscillations. Here, the p values are set to 1.1×10^{-7} and 1.1×10^{-8}, respectively, and the results corresponding to the two p values are obtained by discrete model simulation, as shown in Fig. 18. Compared with the original case in Fig. 13, the oscillation of i_a is significantly reduced after adding the filter, and the available operating range expands as p decreases. This shows that the additional filter method is theoretically effective for suppressing oscillations, provided that the appropriate filter parameters are chosen.

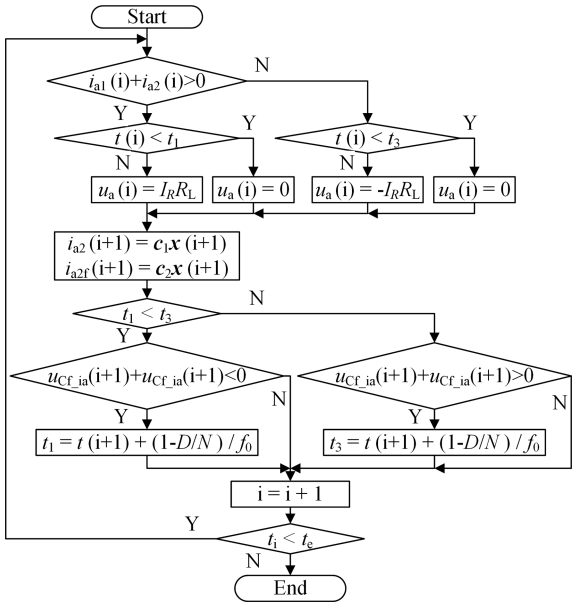

Fig. 17. Flowchart of the improved discrete model.

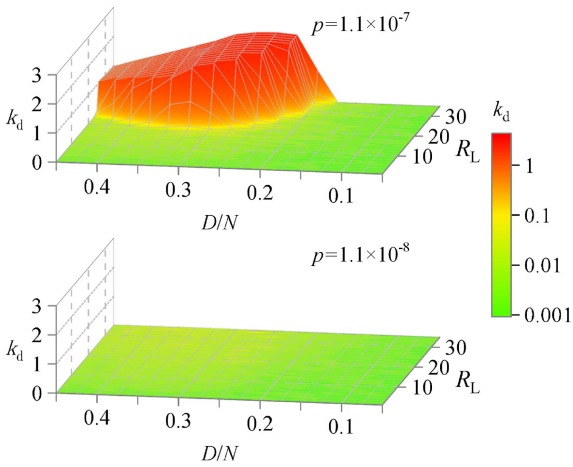

Fig. 18. Values of the simulated k_d at different p.

V. Verification

In order to verify the feasibility of the proposed oscillation suppression method in a practical system, a prototype of the wireless charging system is built, as shown in Fig. 19(a). The prototype consists of a dc source, a full-bridge inverter, an active rectifier, an electronic load, the *LCC-LCC* compensation network, and coupling coils. The schematic of the prototype is shown in Fig. 1, and the resonant network parameters are shown in Table I. The magnetic coupling coils are of square planar helical structure. Each coil consists of Litz wire, ferrite cores, an aluminum plate, and a plastic frame. Table II gives the specific parameters of the coupling coils. The dielectric of the compensation capacitors is polypropylene film, and the detailed parameters of the capacitors are shown in Table III. Fig. 19(b) shows the image of the active rectifier and its various sections.

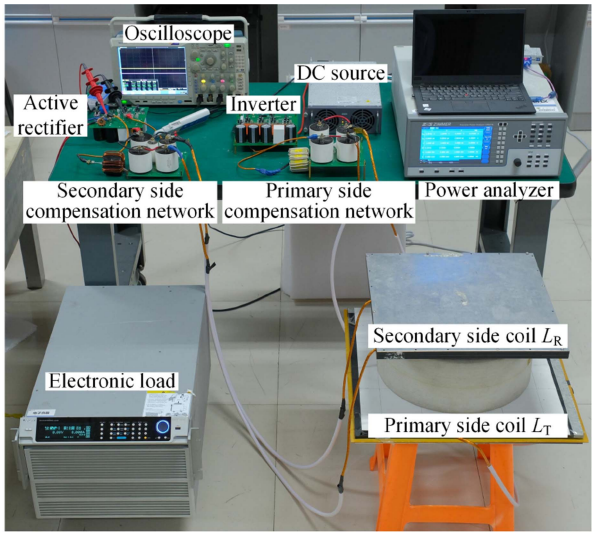

(a)

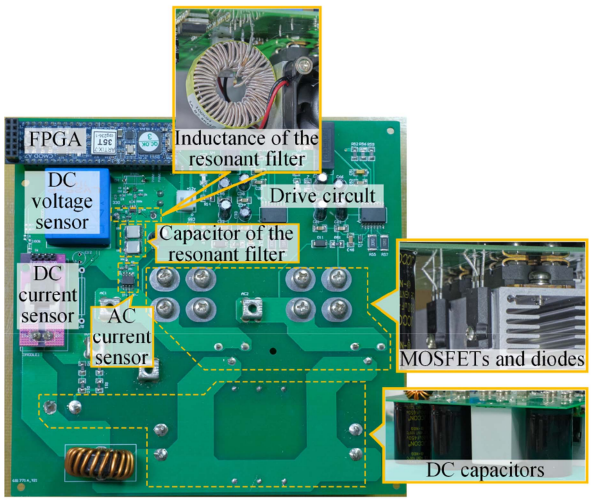

(b)

Fig. 19. Experimental prototype of the WPT system. (a) Entire experimental setup. (b) Active rectifier and its various sections.

TABLE II
PARAMETERS OF THE COUPLING COILS

Parameter	Value
Size of L_T	500 mm × 500 mm
Size of L_R	400 mm × 400 mm
Turns of the L_T	10
Turns of the L_R	16
Spacing between turns	3.5 mm
Number of strands of Litz wire	1800
Single strand diameter of Litz wire	0.10 mm
Distance between coupling coils	200 mm
Ferrite core material	PC95
Size of single ferrite core	100 mm × 100 mm × 10 mm

TABLE III
PARAMETERS OF THE COMPENSATION CAPACITORS

Parameter	Value
Urms	3000 V
Irms	40 A
du/dt	3500 V/μs
ESR@1.0kHz	2 mΩ

TABLE IV
PARAMETERS OF THE EXPERIMENT AND DEVICES

Symbol	Parameter	Value
V_s	Voltage of the dc source	390 V
f_s	Frequency of the inverter	87.5 kHz
k_{sens}	Sensitivity of ACS730KLCTR-40AB-T	50 mV/A
bw	Bandwidth of ACS730KLCTR-40AB-T	1 MHz
t_{pd}	Propagation delay time of TLV3201	40 ns

The power devices of the circuit are SiC MOSFETs (IXFN50N120SiC) and SiC diodes (FFSH40120ADN). The modulation method of the drive signal is shown in Fig. 4, where the sensor ACS730KLCTR-40AB-T is used for the current sensing block, the comparator TLV3201 is used for the zero-crossing comparison block, and the functions of the remaining blocks are all implemented by the FPGA XC7A35T. The experiment and device parameters are shown in Table IV.

A. *Validity of the Proposed Model*

The computational results of the proposed model are compared with the results of the simulation and experiment to verify the validity of the model. The waveforms of i_a for three operating states with $R_L = 9\ \Omega$ and D/N of 0.2, 0.3, and 0.4 are selected from Fig. 13 and presented in Fig. 20. It can be seen that the waveforms of the current are stable when D/N is 0.2 and 0.3, while significant oscillation occurs when D/N is 0.4. Fig. 21 gives the simulation results obtained from the circuit built in Simulink for the same three operating states. Comparing Figs. 20 and 21, it can be seen that the results of the proposed model and simulation are in high agreement, both in stable operation and in the presence of oscillations. Fig. 22(a) and (b) give the experimental waveforms when $R_L = 9\ \Omega$ and D/N is 0.2 and 0.3, respectively, and Fig. 22(c) gives the waveforms when D/N is 0.4 and oscillation occurs. Obviously, the experimental waveforms also match the results of the proposed model. The simulation and experimental verification illustrate that the proposed model is accurate for the calculation of the dynamic process. In particular, the accurate reduction of the oscillation waveform proves that the proposed oscillation loop is correct.

The stable operating range of the prototype is obtained by uniform interval testing. The critical load at which oscillation occurs at each setting is measured by varying the D/N setting in the range of 0.05 to 0.45 at intervals of 0.05, and the oscillation boundary curve is fitted based on the critical data. The experimental results of the original prototype are shown in Fig. 23(a), where α indicates the region where stable operation is not possible. It can be seen that the prototype oscillates in the interval from D/N of 0.15 to 0.45 in the test range. And between 0.2 and 0.4, the load when oscillation occurs is smaller, so the stable operation of the prototype in this interval is most seriously affected by oscillation.

In Fig. 23(b), the oscillation boundary curves in Fig. 13 are compared with the experimental results. It can be seen from Fig. 23(b) that both curves show the same trend, but the experimental curve is higher than the one obtained by the model. This is because the modulation process shown in Fig. 4 is idealized

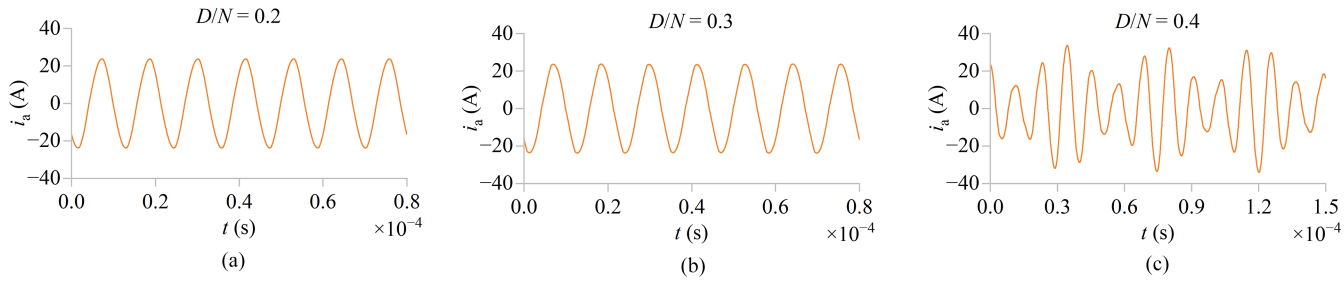

Fig. 20. i_a waveforms obtained from the discrete model. (a) $D/N = 0.2$, $R_L = 9\ \Omega$. (b) $D/N = 0.3$, $R_L = 9\ \Omega$. (c) $D/N = 0.4$, $R_L = 9\ \Omega$.

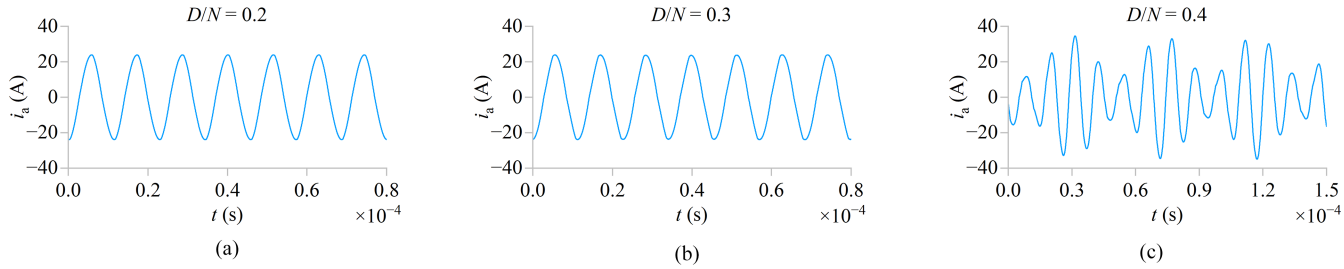

Fig. 21. i_a waveforms obtained in simulink. (a) $D/N = 0.2$, $R_L = 9\ \Omega$. (b) $D/N = 0.3$, $R_L = 9\ \Omega$. (c) $D/N = 0.4$, $R_L = 9\ \Omega$.

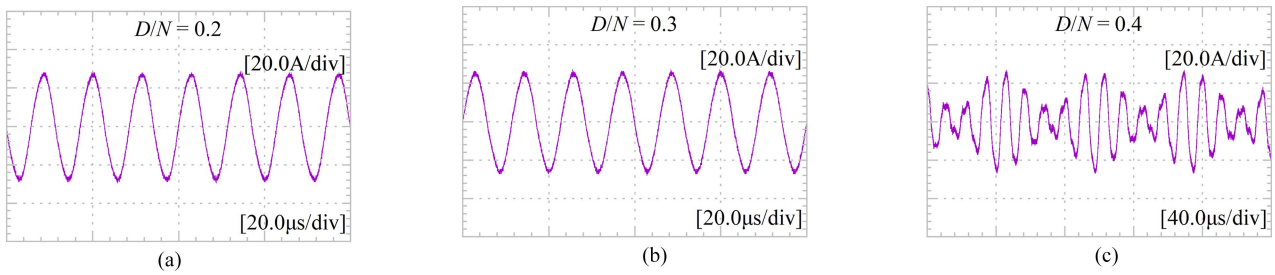

Fig. 22. i_a waveforms of the prototype. (a) $D/N = 0.2$, $R_L = 9\ \Omega$. (b) $D/N = 0.3$, $R_L = 9\ \Omega$. (c) $D/N = 0.4$, $R_L = 34\ \Omega$.

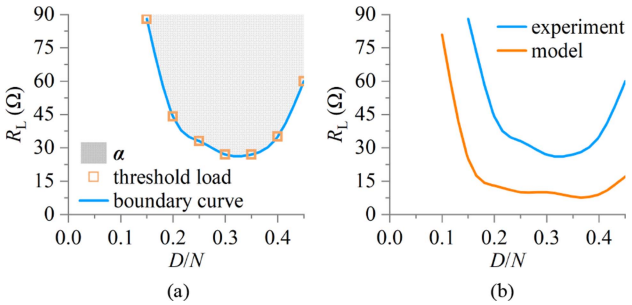

Fig. 23. (a) Range of oscillations of the experimental prototype. (b) Comparison of oscillation boundaries between simulation and experiment.

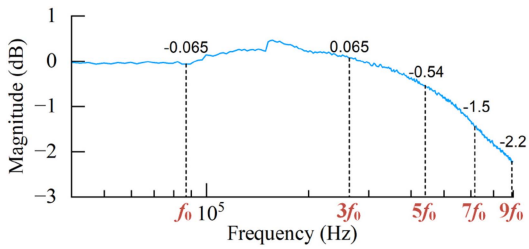

Fig. 24. Amplitude-frequency characteristics curve of ACS730KLCTR-40AB-T.

in the model, while in reality, the devices in this part of the circuit have an impact on the signal transmission due to their electrical characteristics. Among them, the current sensor used in the prototype has a low-pass characteristic, which has a strong attenuation effect above the nominal cutoff frequency, and the amplitude-frequency characteristic curve of the chip is shown in Fig. 24. So the sensor attenuates part of the i_{a2} component to some extent and, according to the previous study, this helps to improve the oscillation problem. Therefore, it is reasonable that the stability region of the prototype in the experiment is larger than the one calculated in the model. As for the comparator and FPGA in the modulation circuit, the effect of these parts is that the transmission delay of the device causes the falling edge lag of the driving signals (G5, G6), which in turn makes the actual on-duty cycle of the MOSFETs slightly higher than the set value. However, the t_{pd} of TLV3201 is only 40 ns, and the

TABLE V
PARAMETERS OF THE ADDITIONAL RESONANT FILTER

Symbol	Parameter	Value
L_f	Inductance of the filter	110 μH
R_{Lf}	Internal resistance of L_f	0.11 Ω
C_f	Capacitor of the filter	30.08 nF
R_f	Resistance of the filter	10 kΩ

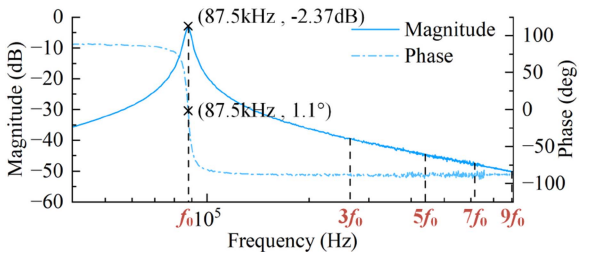

Fig. 25. Measured frequency response of the resonant filter.

transmission delay of FPGA is also in the nanosecond range. The total delay of these two parts is much smaller than the switching period (11.43 μs), so the effect on the duty cycle widening is very small. Consequently, the effect of the comparator and the FPGA can be disregarded. When designing resonant filters to improve oscillations, the larger stable operation region of the actual system makes it more conservative and reliable to use the model results as a reference.

B. Design of the Resonant Filter

The parameters of the resonant filter are designed in the improved prototype. According to the results of Fig. 18, it is clear that the smaller the p, the better the improvement of oscillations. However, there is a limitation on the value of p in the actual circuit. This is because when L_f increases, the consequent increase in the internal resistance R_{Lf} reduces the gain of the filter at the resonant frequency. When considering the internal resistance of L_f, the gain of the filter at ω_0 is

$$G_f(\omega_0) = 1 - \frac{R_{Lf}/L_f}{p(\omega_0^2 - j\omega_0 R_{Lf}/L_f) + R_{Lf}/L_f}. \quad (31)$$

From (31), it can be seen that R_{Lf} causes $G_f(\omega_0)$ to be less than 1. In addition, with fixed core and wire specifications, R_{Lf} has a linear relationship with the self-inductance, thus, R_{Lf}/L_f in (31) can be considered as a constant. In this case, the smaller the p, the more the fundamental signal is attenuated, which is detrimental for the comparator to detect the zero-crossing point of the fundamental signal. In order to achieve a balance, it is necessary to determine the upper limit of p according to the stable operating range desired to be achieved and to determine the lower limit of p in terms of the fundamental signal being able to be accurately detected by the comparator. According to the results shown in Fig. 18, for the system studied in this article, a better improvement can be achieved when $p = 1.1 \times 10^{-8}$, so the p of the prototype filter is designed as 1.1×10^{-8}, and the specific filter parameters are shown in Table V. The measured frequency response of the filter is shown in Fig. 25, where $|G(\omega_0)| = -2.37$ dB. The amplitude of the fundamental component in the filter output is calculated by the following equation:

$$U_{Cf1} = I_{a1} k_{sens} |G_f(\omega_0)|. \quad (32)$$

According to (7), it is calculated that $I_{a1} = 23.5$ A, so $U_{Cf1} = 0.89$ V. Fig. 26 gives the waveforms during operation, where u_{ia} is the current sensor output waveform and u_{Cf} is the filter output waveform. It can be seen that u_{ia} matches i_a and u_{Cf} appears as a sinusoidal waveform, which indicates that the filter achieves sufficient harmonic attenuation effect. The output waveform of the comparator is shown in cmp of Fig. 27, and it can be seen that the comparator can accurately measure the zero-crossing point of u_{Cf}. This shows that the designed filter parameters are reasonable.

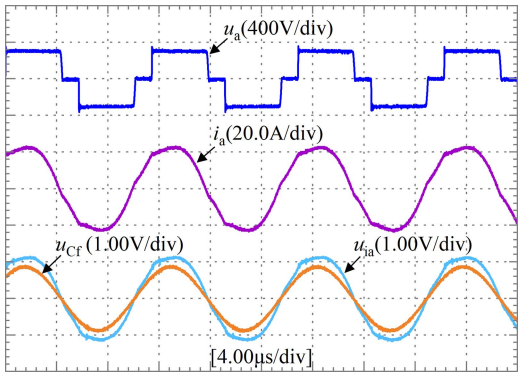

Fig. 26. Waveforms of u_a, i_a, u_{Cf}, and u_{ia}.

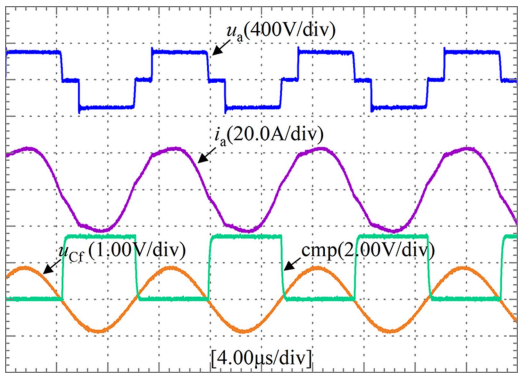

Fig. 27. Waveforms of u_a, i_a, u_{Cf}, and cmp.

C. Experimental Results of the Improved Prototype

The operation of the prototype with the additional resonant filter is tested. To verify the oscillation improvement of the proposed method, the operating parameters on the boundary curve in Fig. 23(a) are selected for testing. Fig. 28 gives the waveforms of the original prototype when D/N is 0.2, 0.3, and 0.4 on the boundary curve, respectively. And Fig. 29 gives the waveforms of the improved prototype. The comparison between Figs. 28 and 29 shows that the oscillation is effectively eliminated after the resonant filter is added.

In order to clarify the influence of the proposed method on the efficiency of the active rectifier, four sets of operating parameters

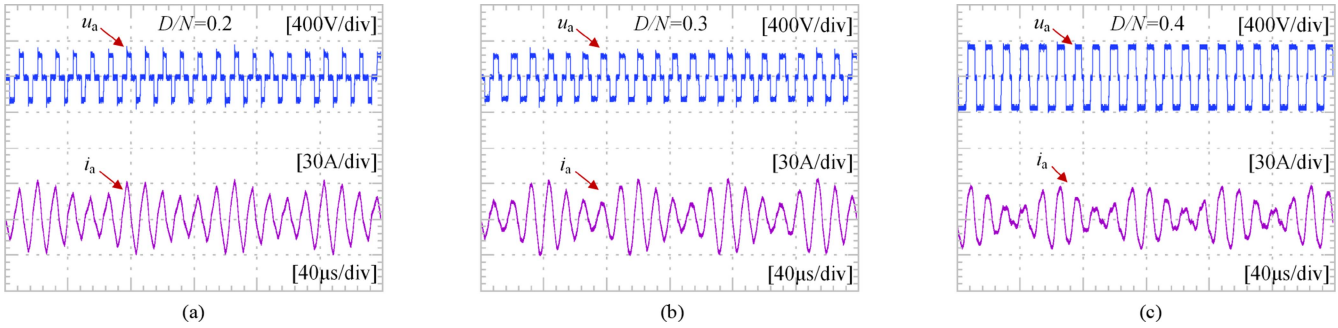

Fig. 28. u_a and i_a waveforms of the original prototype. (a) $D/N = 0.2$, $R_L = 44\ \Omega$. (b) $D/N = 0.3$, $R_L = 27\ \Omega$. (c) $D/N = 0.4$, $R_L = 34\ \Omega$.

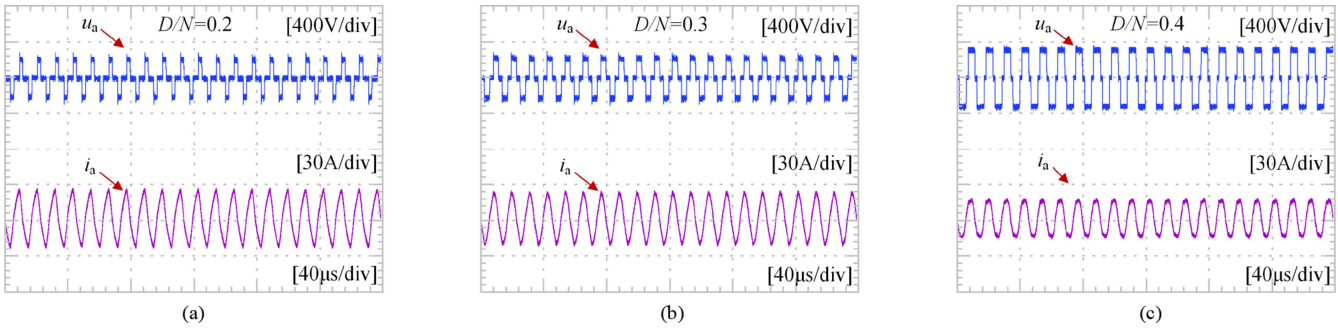

Fig. 29. u_a and i_a waveforms of the improved prototype. (a) $D/N = 0.2$, $R_L = 44\ \Omega$. (b) $D/N = 0.3$, $R_L = 27\ \Omega$. (c) $D/N = 0.4$, $R_L = 34\ \Omega$.

TABLE VI
COMPARISON IN THE EFFICIENCY BETWEEN THE ORIGINAL AND IMPROVED PROTOTYPE

D/N and R_L paraments	Original efficiency	Improved efficiency
$D/N = 0.40$, $R_L = 40\ \Omega$	97.0%	97.0%
$D/N = 0.60$, $R_L = 27\ \Omega$	97.3% (oscillation)	97.6%
$D/N = 0.77$, $R_L = 23\ \Omega$	97.1%	97.1%
$D/N = 0.89$, $R_L = 20\ \Omega$	97.3%	97.3%

are randomly selected for testing. The efficiency of the original and the improved prototype are compared in Table VI. From the test results, at $D/N = 0.60$, $R_L = 27\ \Omega$, the original prototype operated with oscillations, while in the improved prototype the oscillations are eliminated, and the efficiency is increased from 97.3% to 97.6%. The system is always in stable operation in the other three sets of parameters. And the efficiency of the original and the modified prototype is the same for each set of parameters. Given that the resonant filter is added to the modulation circuit rather than to the power loop, there is no increase in power loss. The abovementioned results prove that the added filter does not affect the efficiency.

Furthermore, to obtain a stable operating range for the improved prototype, the prototype continued to be tested with R_L increasing. In the experiment, as R_L is gradually increased to 200 Ω, the oscillation does not appear at any D/N, which means that the stable operating range of the modified prototype is greatly extended, as shown in Fig. 30. The applicability of the active rectifier circuit in real systems is greatly increased. Taking the constant voltage (CV) charging mode commonly

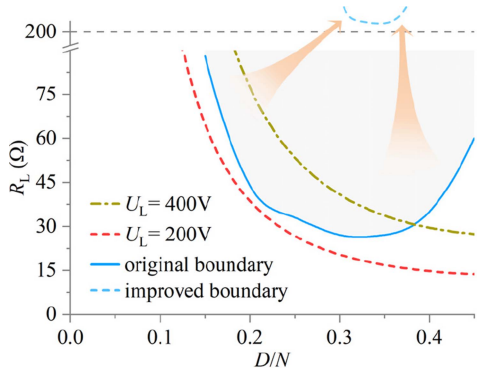

Fig. 30. Comparison of original and improved experimental results.

used in wireless charging of electric vehicles as an example, the trajectory of CV operation can be derived from (5) and Ohm's law equation

$$R_L = \frac{\pi U_L}{I_a\left(1 - \cos\frac{2\pi D}{N}\right)}. \tag{33}$$

Fig. 30 gives the CV mode operation traces of 200 V and 400 V for the prototype in this paper. It can be seen that the unstable operation region of the original prototype is crossed by the 400 V trajectory, so it cannot operate in the constant 400 V mode and can only just meet the CV output of 200 V. In contrast, the range in which the improved prototype can achieve stable operation is already well above the 400 V trajectory curve.

VI. Conclusion

This article illustrates how the controlled rectification operates in the WPT system, and the mechanism of its effect on the zero-crossing point of the secondary-side current is explained. The dynamic influence process between the voltage and current on the secondary side is described. The closed loop formed by PWM modulation and conduction that triggers the oscillation in the system is pointed out. A discrete model of the active rectifier in the WPT system is developed and the dynamic process of the system is simulated. Meanwhile, the oscillations of the system regarding the operating parameters are presented. To solve the oscillation problem, a control method based on an additional resonant filter is proposed to make the PWM modulation independent of the closed loop by attenuating the harmonics in the current sensing signal. Simulation and experimental results demonstrate that the improved control method is effective in eliminating oscillations and extensively improves the range of stable operation in a set of prototypes.

References

[1] J. Park et al., "A resonant reactive shielding for planar wireless power transfer system in smartphone application," *IEEE Trans. Electromagn. Compat.*, vol. 59, no. 2, pp. 695–703, Apr. 2017.

[2] C. You, K. Huang, and H. Chae, "Energy efficient mobile cloud computing powered by wireless energy transfer," *IEEE J. Sel. Areas Commun.*, vol. 34, no. 5, pp. 1757–1771, May 2016.

[3] M. J. Karimi, A. Schmid, and C. Dehollain, "Wireless power and data transmission for implanted devices via inductive links: A systematic review," *IEEE Sensors J.*, vol. 21, no. 6, pp. 7145–7161, Mar. 2021.

[4] S.-J. Huang, T.-S. Lee, W.-H. Li, and R.-Y. Chen, "Modular on-road AGV wireless charging systems via interoperable power adjustment," *IEEE Trans. Ind. Electron.*, vol. 66, no. 8, pp. 5918–5928, Aug. 2019.

[5] C. Zhu et al., "Analysis and design of cost-effective WPT systems with dual independently regulatable outputs for automatic guided vehicles," *IEEE Trans. Power Electron.*, vol. 36, no. 6, pp. 6183–6187, Jun. 2021.

[6] S. Li and C. C. Mi, "Wireless power transfer for electric vehicle applications," *IEEE J. Emerg. Sel. Topics Power Electron.*, vol. 3, no. 1, pp. 4–17, Mar. 2015.

[7] L. Tan, H. Xie, Z. Wu, R. Wang, and X. Huang, "An optimized power-efficiency coordinated control method for EVs charging and discharging applications," *IEEE Trans. Ind. Electron.*, vol. 70, no. 7, pp. 7257–7267, Jul. 2023, doi: 10.1109/tie.2022.3201326.

[8] F. Wen, X. Chu, Q. Li, and W. Gu, "Compensation parameters optimization of wireless power transfer for electric vehicles," *Electronics*, vol. 9, no. 5, p. 789, 2020.

[9] H. Pang, K. T. Chau, W. Liu, and X. Tian, "Multi-resonating-compensation for multi-channel multi-pickup wireless power transfer," *IEEE Trans. Magn.*, vol. 58, no. 8, Aug. 2022, Art. no. 8600506.

[10] S. Li, W. Li, J. Deng, T. D. Nguyen, and C. C. Mi, "A double-sided LCC compensation network and its tuning method for wireless power transfer," *IEEE Trans. Veh. Technol.*, vol. 64, no. 6, pp. 2261–2273, Jun. 2015.

[11] J. Deng et al., "Frequency and parameter combined tuning method of LCC–LCC compensated resonant converter with wide coupling variation for EV wireless charger," *IEEE J. Emerg. Sel. Topics Power Electron.*, vol. 10, no. 1, pp. 956–968, Feb. 2022.

[12] M. Mohammadi and M. Ordonez, "Synchronous rectification of LLC resonant converters using homopolarity cycle modulation," *IEEE Trans. Ind. Electron.*, vol. 66, no. 3, pp. 1781–1790, Mar. 2019.

[13] S. Sinha, A. Kumar, B. Regensburger, and K. K. Afridi, "Active variable reactance rectifier—A new approach to compensating for coupling variations in wireless power transfer systems," *IEEE J. Emerg. Sel. Topics Power Electron.*, vol. 8, no. 3, pp. 2022–2040, Sep. 2020.

[14] W. Li, S. Zong, F. Liu, H. Yang, X. He, and B. Wu, "Secondary-side phase-shift-controlled ZVS DC/DC converter with wide voltage gain for high input voltage applications," *IEEE Trans. Power Electron.*, vol. 28, no. 11, pp. 5128–5139, Nov. 2013.

[15] K. Colak, E. Asa, M. Bojarski, D. Czarkowski, and O. C. Onar, "A novel phase-shift control of semibridgeless active rectifier for wireless power transfer," *IEEE Trans. Power Electron.*, vol. 30, no. 11, pp. 6288–6297, Nov. 2015.

[16] R. Mai, Y. Liu, Y. Li, P. Yue, G. Cao, and Z. He, "An active-rectifier-based maximum efficiency tracking method using an additional measurement coil for wireless power transfer," *IEEE Trans. Power Electron.*, vol. 33, no. 1, pp. 716–728, Jan. 2018.

[17] H. Li, J. Xu, F. Gao, Y. Zhang, X. Yang, and H. Tang, "Duty cycle control strategy for dual-side LCC resonant converter in wireless power transfer systems," *IEEE Trans. Transp. Electrific.*, vol. 8, no. 2, pp. 1944–1955, Jun. 2022.

[18] M. Zhang, L. Tan, J. Li, and X. Huang, "The charging control and efficiency optimization strategy for WPT system based on secondary side controllable rectifier," *IEEE Access*, vol. 8, pp. 127993–128004, 2020.

[19] Y. Jiang et al., "Phase-locked loop combined with chained trigger mode used for impedance matching in wireless high power transfer," *IEEE Trans. Power Electron.*, vol. 35, no. 4, pp. 4272–4285, Apr. 2020.

[20] S. Zhao, Y. Li, D. Wu, and R. Mai, "Current-decomposition-based digital phase synchronization method for BWPT system," *IEEE Trans. Power Electron.*, vol. 36, no. 11, pp. 12183–12188, Nov. 2021.

[21] B. Shi, F. Yang, C. Hu, and M. Ouyang, "Modelling and improvement of oscillation problem in a double-sided LCC compensation network for electric vehicle wireless power transfer," *ETransportation*, vol. 8, 2021, Art. no. 100108.

[22] R. Wang, L. Tan, C. Li, T. Huang, H. Li, and X. Huang, "Analysis, design, and implementation of junction temperature fluctuation tracking suppression strategy for SiC MOSFETs in wireless high-power transfer," *IEEE Trans. Power Electron.*, vol. 36, no. 1, pp. 1193–1204, Jan. 2021.

[23] D. J. Thrimawithana, U. K. Madawala, and M. Neath, "A synchronization technique for bidirectional IPT systems," *IEEE Trans. Ind. Electron.*, vol. 60, no. 1, pp. 301–309, Jan. 2013.

[24] X. Liu, N. Jin, X. Yang, T. Wang, K. Hashmi, and H. Tang, "A novel synchronization technique for wireless power transfer systems," *Electronics*, vol. 7, no. 11, p. 319, 2018.

[25] Y. Tang, Y. Chen, U. K. Madawala, D. J. Thrimawithana, and H. Ma, "A new controller for bidirectional wireless power transfer systems," *IEEE Trans. Power Electron.*, vol. 33, no. 10, pp. 9076–9087, Oct. 2018.

[26] C. Xia, R. Chen, Y. Liu, L. Liu, and G. Chen, "Inhibition of current harmonics in LCL/LCC wireless power transfer system," in *Proc. IEEE Power Electron. Soc. Workshop Emerg. Technol., Wireless Power Transfer*, 2017, pp. 1–6.